

# Morphology Evolution during Delithiation of Li-Pb Alloys: Oscillatory Electrochemical Behavior

Ke Geng, Minglu Liu, Yusi Xie, Ashlee Aiello,\* Erin Karasz, and Karl Sieradzki Oz

Fulton School of Engineering, Arizona State University, Tempe, Arizona 85287, USA

We report on a study of morphology evolution following de-lithiation of Li-Pb alloys, produced by the electrochemical lithiation of Pb particulate and sheet electrodes. Electrochemical titration and time of flight measurements were performed in order to determine the intrinsic diffusivity of Li,  $\bar{D}_{Li}$ , as a function of alloy composition, which ranged from  $10^{-12}$ – $10^{-10}$  cm<sup>2</sup>s<sup>-1</sup>. Morphology evolution was studied under conditions of galvanostatic and potentiostatic dealloying. For the particulate electrodes, we observed dealloyed morphologies corresponding to Kirkendall voids, negative dendrites, void nodules and conventional bicontinuous nanoporous structures. In the case of Pb sheets, similar dealloyed morphologies were obtained under galvanostatic dealloying conditions, however, in the case of potentiostatic dealloying, we did not observe the formation of large volume bicontinuous nanoporous structures. For Pb sheets lithiated to a composition corresponding to the Li<sub>8</sub>Pb<sub>3</sub> phase and galvanostatically dealloyed at current densities ~1 mAcm<sup>-2</sup>, voltage oscillations were observed with periods of 70–90 s and amplitudes ranging from 20–130 mV. Current oscillations were also observed for potentiostatic dealloying at 1 V vs Li<sup>+</sup>/Li. The possible mechanism of these oscillations is discussed and attributed to a salt film precipitation and lift-off process.

© The Author(s) 2019. Published by ECS. This is an open access article distributed under the terms of the Creative Commons Attribution 4.0 License (CC BY, http://creativecommons.org/licenses/by/4.0/), which permits unrestricted reuse of the work in any medium, provided the original work is properly cited. [DOI: 10.1149/2.0161906jes] (cc) BY

Manuscript submitted January 10, 2019; revised manuscript received March 7, 2019. Published March 16, 2019.

The ambient temperature dealloying of noble-metal alloys such as Ag-Au, Cu-Au, Ni-Pt and Cu-Pt has been studied in detail over the past 40 years. 1-8 In these alloys, when the concentration of the noblemetal component is in the range of 20-35 at.%, selective dissolution of the more electrochemically reactive element results in self-organized nanoporous structures. The relevant transport processes during dealloying include surface diffusion and mass transport in the liquid phase containing the dissolved cation species. At ambient temperature, solidstate mass transport is far too slow to contribute to the self-organization process. Transport in the liquid phase can become important if the dissolution flux is larger than what can be accommodated by liquidphase mass transport. Under this condition the concentration of the dissolving species will increase at the solid/liquid interface and eventually the solubility of the dissolving species in the electrolyte could be exceeded, which can result in precipitation of a salt film and oscillatory electrochemical signals. 10 Kinetic Monte Carlo simulations have demonstrated that surface diffusion is the dominant transport process during self-organization of the nanoporous morphology. 1,6 This morphology is finding applications in a diverse range of applications including catalysis, sensing and actuation.5,11-21

In comparison, there has been relatively little work aimed at examining dealloying under conditions for which solid-state bulk diffusion can significantly contribute to transport and morphology evolution. Geng and Sieradzki briefly reviewed this research in a manuscript examining dealloying in the Li-Sn system.<sup>22</sup> For the Li-Sn system they found that bi-continuous morphologies formed for alloys containing more than 50 at.% Li at potentials larger than a compositionally dependent critical potential. For alloys containing less Li, and at high enough potentials, they observed negative dendrite structures while at lower potentials they reported the occurrence of Kirkendall voiding. The latter two morphologies were associated with solid-state diffusion-limited dealloying. Similar results were reported by Chen and Sieradzki.<sup>23</sup> In this manuscript, we report on dealloying in the Li-Pb system. The thermodynamic phase diagrams for Li-Sn and Li-Pb are similar. According to the equilibrium phase diagrams, the highest melting point alloys in these systems are Li<sub>7</sub>Sn<sub>2</sub> and Li<sub>7</sub>Pb<sub>2</sub> which have melting temperatures of 1056 K and 999 K respectively, whereas elemental Sn and Pb have melting points of 565 K and 601 K.<sup>24,25</sup> In these alloys systems, the highest concentration intermetallic is Li<sub>22</sub>M<sub>5</sub> (M = Sn, Pb); both have a cubic structure and identical space groups.<sup>26</sup>

Recently, Wood et al. examined the electrochemical lithiation (to 5 mV vs Li<sup>+</sup>/Li) and de-lithiation (to 1.00 V vs Li<sup>+</sup>/Li) of Li-Pb

in 1M LiPF<sub>6</sub> in fluoroethylene carbonate.<sup>27</sup> The Pb electrodes were comprised of  $\sim$ 150  $\mu$ m-sized particles (100 mesh), mixed with a binder and coated on to a copper current collector. They determined the phases present as a function of potential using ex situ X-ray diffraction and identified the presence of LiPb, Li<sub>8</sub>Pb<sub>3</sub>, Li<sub>3</sub>Pb and Li<sub>7</sub>Pb<sub>2</sub>. Other phases present in the equilibrium phase diagram were not observed.

In this manuscript we examine the dealloying behavior of Li-Pb alloys using methods similar to those used by Geng and Sieradzki to examine the behavior of the Li-Sn alloy system. 22 Some of our results are similar to those found for the Li-Sn system, however, we observed significantly different potentiostatic dealloying behavior and morphology evolution. Notably, we also observed electrochemical oscillatory behavior. To our knowledge, there has only been one previous report of oscillatory current/voltage behavior during dealloying of Li alloys.<sup>28</sup> That work examined lithiation and de-lithiation behaviors in surface modified Li<sub>4</sub>Ti<sub>5</sub>O<sub>12</sub> particulate electrodes in 1M LiTFSI dissolved in a 1:1 electrolyte of ethylene carbonate and dimethyl carbonate. The amplitude of the voltage oscillations was in the range of 1-10 mV and the period of oscillation was  $\sim$ 150–200 s (estimated from C-rate discharge voltage - capacity data). These oscillations were attributed to a coupled "particle-by-particle" phase separation process. Mosaic instabilities and voltage fluctuations during de-lithiation of particulate electrodes have been predicted to occur at low currents in a modified porous electrode theory using phase field simulations.<sup>29</sup>

# Methods

All electrochemical measurements and morphology evolution experiments were conducted inside an ultrahigh-purity argon-purged MBraun LABMaster glove box ( $\rm H_2O$  and  $\rm O2 < 0.1$  ppm) using either a Gamry series-G or BioLogic SP-150 potentiostat. All potentials reported in this work are versus a Li<sup>+</sup>/Li quasi-reference electrode.

Sample preparation.—Pb foils (United Metal & Chemical Corp., 5N purity) were cold rolled to 0.0005" (12.7  $\mu$ m) and shelf-stored at room temperature before use. Li foils (thickness = 0.75 mm, 99.9%, Alfa Aesar) were used as received.

Pb particles with nominal diameter of 1  $\mu m$  were made following Wang and Xia's procedure  $^{30}$  with an increased amount of lead acetate and decreased amount of poly(vinyl pyrrolidone) (PVP). Lead acetate (0.94837 g) dissolved in 5 mL tetraethylene glycol (TEG) was added dropwise to 20 mL of boiling TEG solution with PVP (0.1 g PVP/10 mL TEG) in a 100 mL three-neck round-bottom flask, which was kept in an inert environment under a continuous flow of Ar. The reaction mixture was stirred for 15 minutes and quenched into cold

<sup>\*</sup>Electrochemical Society Student Member.

<sup>&</sup>lt;sup>z</sup>E-mail: KARL.SIERADZKI@asu.edu

ethanol (at dry ice temperature;  $-78.5^{\circ}$ C). The black-brownish precipitates were harvested and cleaned by centrifuging with ethanol three times. The product was air-dried at room temperature overnight to remove the residual ethanol. The size of the resultant Pb micro-particles was confirmed by scanning electron microscopy. These Pb particles were mixed with Super-C45 carbon black (TIMCAL) and polyvinylidene fluoride (Sigma Aldrich) in a 5:3:2 weight ratio in N-methyl-2-pyrrolidone (Sigma Aldrich). The as-mixed slurry was pasted onto a copper substrate creating a layer of thickness a few microns, and dried under flowing  $N_2$  at  $60^{\circ}$ C, to maintain the size, shape and particle separation.

Pb particles with diameter of 5 or 15  $\mu m$  were galvanostatically electrodeposited from 0.1 mol/L Pb(ClO<sub>4</sub>)<sub>2</sub> + 0.1 mol/L HClO<sub>4</sub> on well-polished Cu disks at a current density of 2.5 mAcm<sup>-2</sup> for 250 or 600 s, respectively. The mean size of the electrodeposited particles was determined using SEM.

Lithiation/de-lithiation.—Lithiation-delithiation of Pb foils and Pb particles on Cu disks was conducted in a 3-neck round-bottom flask cell containing 10 mL of 1 M LiClO<sub>4</sub> in polypropylene carbonate. Two pieces of Li foil were used as the counter and reference electrodes. The Pb foils had an active area of 0.25 cm<sup>2</sup> that directly faced the Li foil counter electrode. For the  $\sim 1 \mu m$  diameter Pb particles, electrochemical experiments were performed in a two-electrode pouch cell configuration. The working electrode and Li foil were separated by a glass fiber separator, which was soaked in the electrolyte of 1 M LiPF<sub>6</sub> in diethylene carbonate, dimethylene carbonate, ethylene carbonate in a 2:1:2 ratio by volume (MTI corp.). The Pb particle working electrode, glass fiber separator and Li counter electrode were sealed into a pouch cell under Ar. Potentiostatic lithiation and delithiation was performed by maintaining the working electrode at a prescribed potential until the current density was lower than 10 µAcm<sup>-2</sup>. Galvanostatic lithiation was performed at charging current density of 20  $\mu$  Acm<sup>-2</sup>. Delithiation was performed by discharging at prescribed current densities, until the potential reached 2.5 V (the upper limit in these experiments).

Potentiostatic intermittent titration (PITT)<sup>31</sup> and galvanostatic intermittent titration (GITT)32 measurements.—Pb thin films of thickness 500 nm were vapor deposited on a Cu foil substrate and used as the working electrode in the PITT and GITT measurements. The thickness of these films was confirmed by a profilometer (Bruker Dektak XT). In order to minimize deformation of the Pb/Cu working electrode during lithiation and delithiation, the electrode was fixed to a piece of mica with Kapton tape leaving an exposed area of 0.25 cm<sup>2</sup>. Two pieces of Li foil were used as the counter and reference electrode. A 3-neck round-bottom flask containing 10 mL of 1 M LiClO<sub>4</sub> in polypropylene carbonate was used as the reservoir. Before GITT and PITT experiments, the working electrode was maintained at voltage of 1 V vs. Li<sup>+</sup>/Li until the current density decayed below 10 μAcm<sup>-2</sup>. The GITT procedure consisted of 250 µAcm<sup>-2</sup> pulses for 50 s, followed by a relaxation duration of 100 s. For the PITT measurements, 10 mV potential steps were used and the current was measured as a function of time. The potential was stepped in 10 mV increments either until the current density decayed to 10  $\mu$ Acm<sup>-2</sup> or if the titration time exceeded 5000 s.

Devanathan-Stachurski, (DK), cell measurements<sup>33</sup>.—As described in the original work by Devanathan and Stachurski. The electrochemical cell consisted of two cylindrical glass compartments sealed at the bottom by two size 12 O-ring joints, between which a Pb foil of thickness 15.2 μm and active area of 0.196 cm² (diameter of 0.50 cm) was sandwiched. The Pb foil served as a shared working electrode for both compartments. Each compartment carried two pieces of Li foil serving as reference and counter electrodes. The cathodic side of the Pb foil was potentiostatically lithiated at a voltage of 400 mV, while the anodic side of the Pb foil was maintained at a fixed voltage corresponding to the open circuit potential of Pb insuring that Li could be oxidized to Li<sup>+</sup>. Both compartments were filled with 100 mL of

1 M LiClO<sub>4</sub> in polypropylene carbonate. Potentiostats connecting to both compartments were operated in a floating mode.

Focused ion-beam milling and SEM.—After delithiation, Pb foils were immersed in acetonitrile to remove the SEI layer and then transferred into the SEM chamber. The air exposure was less than 5s when transferred into SEM chamber. SEM and focused ion-beam milling was conducted in a dual-beam Nova 200 NanoLabUHRFEG system at a 52° tilt angle.

#### Results

The composition-dependent diffusion coefficients,  $\bar{D}_{Li}$ , of Li in Pb and Li-Pb alloys were measured using potentiostatic intermittent titration (PITT)<sup>31</sup> and galvanostatic intermittent titration (GITT)<sup>32</sup> techniques as well as a time of flight technique based on the Devanathan-Stachurski cell.<sup>33</sup> PITT and GITT measure the diffusion coefficient by imposing numerous activation-relaxation cycles. During an activation stage, a potential pulse (PITT) or a current pulse (GITT) is applied to introduce a Li concentration gradient in the sample. In the relaxation stage, the Li gradient drives solid-state diffusion, and results in a current decay (PITT) or a potential change (GITT) until a quasi-steady state is reached. In each cycle, the current and potential profiles recorded in the relaxation stage are used to calculate a diffusion coefficient. As the cycle number increases, the host is changing in composition, and the composition-dependent diffusion coefficients are determined. One should note that these titration techniques only apply to single-phase regions, where the equilibrium potential is strictly compositional-dependent. In a two-phase coexistence region, this dependence breaks down, and the calculated diffusion coefficient can significantly underestimate the true value because the current is consumed by both new phase formation and Li diffusion (PITT), or in the case of GITT, the electrochemical potential is constant in the two-phase regions.

In this work, the diffusion coefficients were calculated using Equations  $1^{31}$  and  $2^{32}$  for GITT and PITT measurements, respectively. In Equation 1,  $V_M$  is the molar volume of the sample, I is the applied current,  $Z_{Li}=1$  is the charge number, F is Faraday's constant, A is the area of the electrode,  $dE_s/d\delta$  is the slope of steady-state cell potential  $(E_s)$  vs. stoichiometric charge of  $\text{Li}_\delta \text{Pb}$ ,  $dE_t/d\sqrt{1}$  is the slope of transient cell potential vs  $\sqrt{1}$  for each current-on period. In Equation 2, L is the thickness of the Pb layer (here  $L=0.5~\mu\text{m}$ ) and  $\Delta Q$  is the charge accumulated during each potentiostatic step.

$$\bar{D}_{Li} = \frac{4}{\pi} \left( \frac{IV_M}{Z_{Li}FA} \right)^2 \left[ \left( \frac{dE_s}{d\delta} / \frac{dE_t}{d\sqrt{t}} \right) \right]^2$$
 [1]

$$\bar{D}_{Li} = \pi L^2 \left(\frac{I\sqrt{t}}{\Delta O}\right)^2$$
 [2]

A "time of flight" technique developed by Devanathan and Stachurski³³³ was also used to measure a "mean composition" diffusion coefficient,  $< D_{Li} >$ , of Li. In this measurement, the two sides of a Pb foil (of thickness,  $L=15.2~\mu m$ ) served as cathode and anode and a potential of 400 mV is maintained on the input side of the foil (cathode) while a potential of 2.5 V was maintained on the exit side of the foil (anode). The cathodic and anodic currents were measured, and the time lag given by Equation 3 was used to determine the Li diffusion coefficient. The time lag is defined as the time at which the current reaches 0.63 of the steady-state anodic current density.³³

$$\langle D_{Li} \rangle = \frac{L^2}{6t_{Lag}}$$
 [3]

Figure 1A, shows the quasi-equilibrium potentials as a function of Li composition and Fig. 1B shows the differential capacity. The results for the composition-dependent diffusion coefficient,  $\bar{D}_{Li}$ , as a function of potential, E, obtained at ambient temperature from the GITT and PITT measurements for the lithiation and delithiation directions are

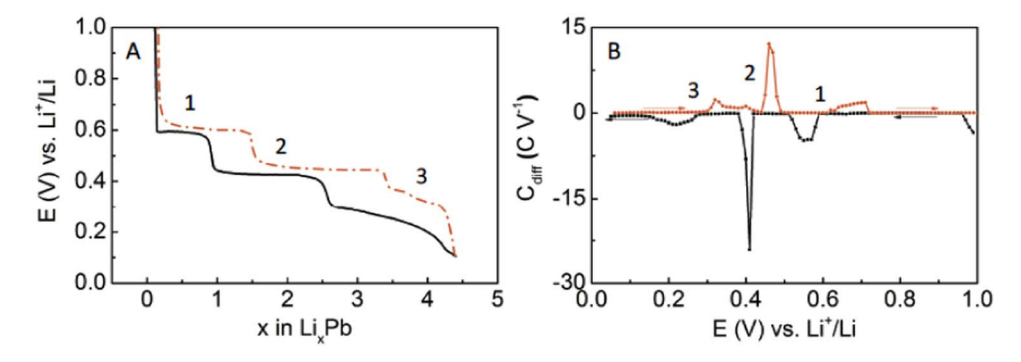


**Figure 1.** Relationship of phase transformation reactions with electrode potential obtained from PITT and GITT measurements on vapor deposited 500 nm-thick Pb on Cu foil. A. The quasi-equilibrium potential of Li-Pb alloys obtained by GITT measurements. B. Differential capacitance as a function of potential obtained by PITT measurement. In these plots the lithiation corresponds to the black curves and de-lithiation the red curves. The two-phase regions are indicated as 1, Pb-LiPb; 2, LiPb – Li<sub>8</sub>Pb<sub>3</sub>; 3, Li<sub>8</sub>Pb<sub>3</sub> – Li<sub>7</sub>Pb<sub>2</sub>.

compared in Figures 2A and 2B. Large decreases in diffusion coefficients were found in the two-phase phase co-existence regions, hence only those in the single-phase regions are taken into consideration. The differences between the PITT and GITT measurements were less than a factor of 1000 and 10 in the lithiation and delithiation direction, respectively. Considering both the GITT and PITT measurements, the diffusion coefficients are of order  $10^{-13}$ – $10^{-12}$  cm<sup>2</sup>s<sup>-1</sup> in the lithiation direction and  $10^{-12} - 10^{-10}$  cm<sup>2</sup>s<sup>-1</sup> in the delithiation direction. One typical current response of Devanathan-Stachurski cell measurement is shown in Fig. 2C. The diffusion coefficient obtained from this measurement was  $1.4 \times 10^{-11}$  cm<sup>2</sup>s<sup>-1</sup>, which is in good agreement with the GITT and PITT results for delithiation. It should be noted that the solid-state diffusion of Li is fast enough to contribute to dealloying at ambient temperature. For example, consider an average diffusion coefficient of Li 10<sup>-12</sup> cm<sup>2</sup>s<sup>-1</sup>, corresponding to a diffusion length of 30 µm within 10<sup>5</sup>s, a time scale commonly used in dealloying of noble-alloys.

Figure 3 shows the morphology obtained for the  $1\mu m$  and  $15 \mu m$  diameter Pb particles lithiated to  $50 \, \text{mV}$  vs.  $\text{Li}^+/\text{Li}$  and delithiated galvanostatically at the indicated C-rate. Typical nanoporous morphologies (Figs. 3A and 3C) were obtained with a mean ligament diameter of order  $50 \, \text{nm}$ . Figure 3B shows a negative dendrite morphology and Fig. 3D shows void nodules. Similar morphologies were observed in the de-lithiation of Li-Sn alloys.

We examined the effect of composition on morphology evolution by potentiostatically dealloying Li-Pb alloy sheets with varying Li concentrations at 2V. Figure 4 show the resultant morphologies with starting compositions of 20, 50, 70 and 75 at.% Li. The quasi-equilibrium potentials and the differential capacitance data in Figure 1 allow us to make the following identifications of the alloy phases likely present at these compositions: Pb and LiPb at 20 at.% Li, LiPb and Li<sub>8</sub>Pb<sub>3</sub> at 50 at.% Li, Li<sub>8</sub>Pb<sub>3</sub> and Li<sub>3</sub>Pb at 70 at.% Li, Li<sub>3</sub>Pb and Li<sub>7</sub>Pb<sub>2</sub> at 75 at.% Li. At first glance, aside from the 20 at.% alloy, the deal-

loyed morphologies are similar except that with increasing Li composition, the pores get smaller and the pore density increases. The morphology that we observe in Figure 4 is not reminiscent of typical bi-continuous nanoporous morphologies obtained during dealloying of Li-Sn alloys<sup>22,23</sup> or noble-metal alloys. <sup>1,9</sup> Henceforth, we will refer to this morphology as "nanoporous void nodule" (NVN) to distinguish it from the conventional large-volume nanoporous morphologies. This indicates that significant spatial compositional inhomogeneity likely exists in the as lithiated Pb sheets.

Figure 5 shows representative morphologies and the associated chronopotentiometry obtained for dealloying of Li-rich alloys at fixed current density. At current densities less than  ${\sim}500~\mu\text{Acm}^{-2},$  negative dendrite morphologies form, while at current densities of  $10~\text{mAcm}^{-2}$  or greater conventional bi-continuous nanoporous morphologies evolve. At a current density of  ${\sim}1~\text{mAcm}^{-2}$  we observe voltage oscillations.

We explored the conditions under which electrochemical oscillations occur. Figure 6 shows representative parameters for which we observed both voltage and current oscillations. Generally, the oscillations require alloys that contain at least 70 at.% Li. Under galvanostatic conditions they were present at current densities  $\sim 1 \text{ mAcm}^{-2}$ . The chronopotentiometry showed that the oscillations occurred between 0.8-1.0 V (vs. Li<sup>+</sup>/Li), with a period  $\sim$ 70–90 s and peak amplitudes (ignoring the initiation stage) ranging from  $\sim$ 20–130 mV. As can be seen in Figure 6, the oscillations in potential always initiated with several larger amplitude, long period spikes that gradually decayed prior to establishing a regular frequency. The details and general appearance of the oscillations were very sensitive to the initial conditions (alloy composition, imposed current density or voltage), i.e., for nominally the same imposed voltage or current different types of oscillations were observed. Under potentiostatic dealloying, current oscillations were observed at voltages of 0.8-1.0 V (vs. Li<sup>+</sup>/Li), with a period  $\sim$ 40–70 s and peak amplitudes ranging from  $\sim$ 10–15  $\mu$ Acm<sup>-2</sup>.

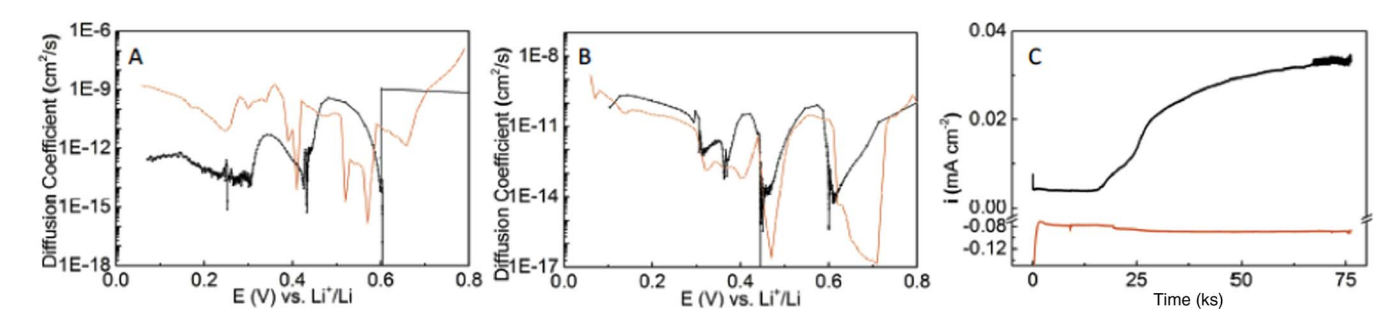


Figure 2. Results of PITT, GITT and DS measurements on the Li diffusivity in Pb at ambient temperature. A. Lithiation and B. de-lithiation directions. GITT result, black line and PITT result red line. C. DS measurement for a 15.2 μm-thick Pb sheet showing current on the cathodic (charging) side (red) and anodic (discharge) side (black).

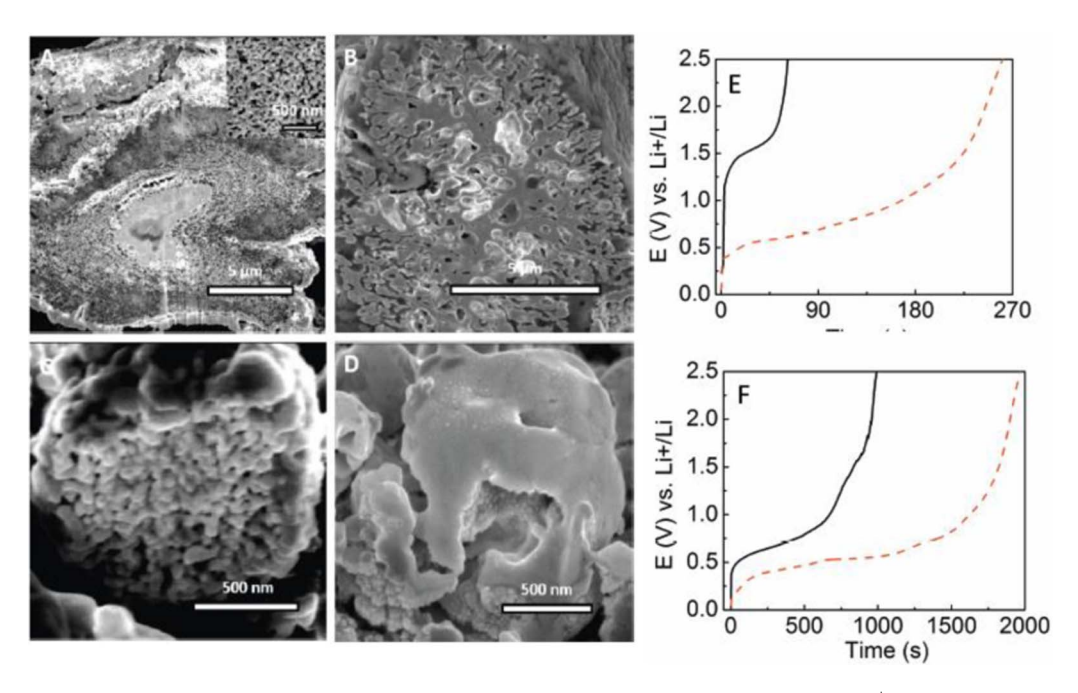
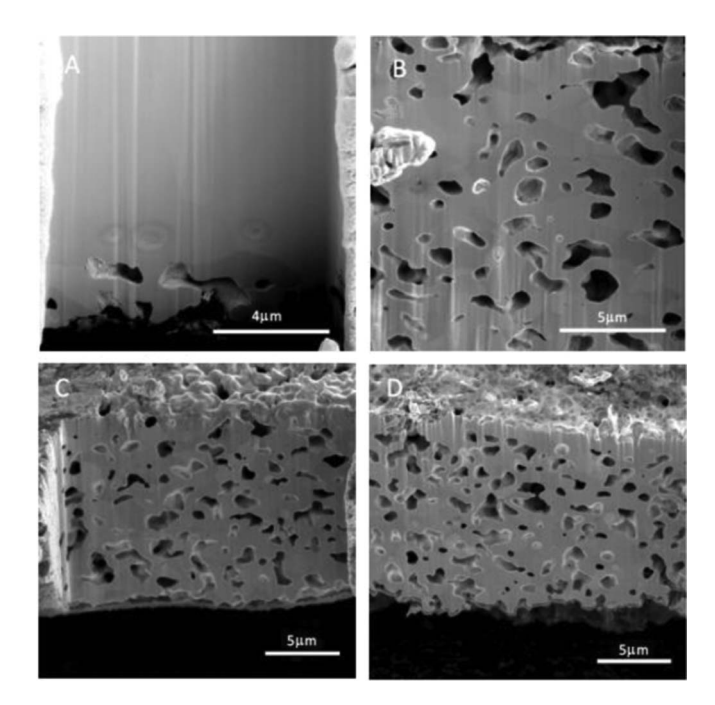


Figure 3. SEMs of FIB cross-sections and chronopotentiometry of Pb particles potentiostatically lithiated to 50 mV vs. Li<sup>+</sup>/Li followed by galvanostatic dealloying at the indicated C rate. A. 60 C; solid core and a bi-continuous porous shell in a  $\sim$ 15  $\mu$ m diameter particle. Inset shows magnified view. B. 18/5 C; negative dendrite and void nodules in a  $\sim$ 15  $\mu$ m diameter particle. C. 15 C; bi-continuous porosity in a  $\sim$ 1  $\mu$ m diameter particle. D. 9/5 C; void nodules in a  $\sim$ 1  $\mu$ m diameter particle. E. Voltage-time profile corresponding to bi-continuous porosity in A (black solid curve) and C (red dashed curve). F. Voltage-time profile corresponding to negative dendrites in B (black solid curve) and void nodule formation in D (red dashed curve).

In order to understand the effect of sample size on morphology evolution during potentiostatic dealloying, particulate and planar sheet Pb hosts were lithiated to 50 mV vs. Li<sup>+</sup>/Li corresponding to the Li<sub>7</sub>Pb<sub>2</sub> composition. These lithiated hosts were potentiostatically delithiated at potentials larger than the equilibrium potential of the LiPb phase (0.6 V vs. Li<sup>+</sup>/Li) and lower than the elemental Pb dissolution potential ( $\sim$ 2.5 V vs. Li<sup>+</sup>/Li) in this electrolyte. As shown in Figure 7A, FIB cross-sections of delithiated 1  $\mu$ m diameter Pb particles show a



**Figure 4.** SEMs of FIB cross-sections of dealloyed Pb sheets potentiostatically lithiated to the indicated atom percent and dealloyed at 2 V vs. Li<sup>+</sup>/Li. A. Li<sub>20</sub>Pb<sub>80</sub>, B. Li<sub>50</sub>Pb<sub>50</sub> C. Li<sub>70</sub>Pb<sub>30</sub> D. Li<sub>75</sub>Pb<sub>25</sub>.

bicontinuous nanoporous morphology. However, no such full-volume morphology evolved in Pb particles of diameter 15  $\mu m$  or Pb sheets of thickness 12.7  $\mu m$  even when dealloying was performed at 2 V vs Li<sup>+</sup>/Li. FIB cross-sections of delithiated 15  $\mu m$  Pb particles show negative dendrite structures (Fig. 7B). Formation of negative dendrite morphologies indicates that the rate of dealloying in these particles was controlled by solid-state diffusion. Figure 7C shows a NVN morphology that evolved in the 12.7  $\mu m$  thick sheets. Close examination of the "walls" of these nodules showed regions of conventional dealloyed nanoporous morphologies (see inset of Fig. 7C).

#### Discussion

We note that SEMs of FIB sections of the pristine Pb electrodes showed no morphology (e.g. voids, porosity, etc.) other than grain boundaries in the Pb sheets. In comparing our results for Li-Pb with dealloying and morphology evolution in the Li-Sn system<sup>22</sup> (for alloys containing more than 70 at.% Li), there were two unexpected findings. In potentiostatic dealloying of Pb sheets, we were unable to obtain typical full volume nanoporous structures regardless of the composition and voltage. As shown in Figures 5C and 5D, under galvanostatic dealloying, conventional nanoporous structures were observed for current densities larger than ~10 mAcm<sup>-2</sup>. In the case Li-Sn alloys, conventional nanoporous structures were formed under galvanostatic dealloying conditions at current densities of only  $\sim 500 \,\mu$  Acm. <sup>22</sup> Under potentiostatic dealloying of Li-Sn at a sufficiently high voltage, these current densities were maintained for thousands of seconds and full volume nanoporous structures were formed.<sup>22</sup> Under potentiostatic dealloying of Li-Pb, we observed NVN morphologies as shown Figure 4. While spatial compositional heterogeneity undoubtedly exists within the lithiated Pb sheets, we reject this as the entire explanation for the NVN morphology given the galvanostatic results (Figs. 5C, 5D). In order to explore this issue, we examined the chronocoulometry at various dealloying potentials for a composition corresponding to Li<sub>8</sub>Pb<sub>3</sub>. As shown in Figure 8, these results revealed that under potentiostatic dealloying, a current density of order 10 mAcm<sup>-2</sup> or higher was maintained only for times ranging from  $\sim$ 20–40 s. This then appears to be at least part of the explanation. Another part of

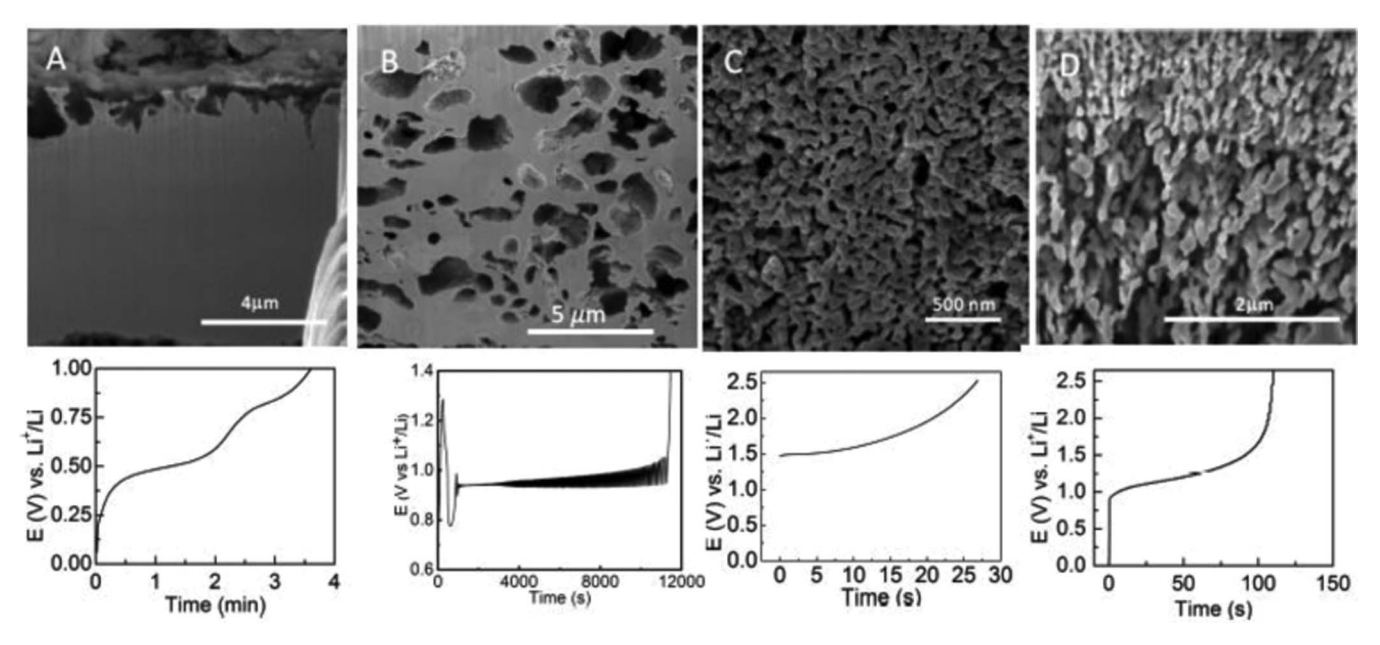
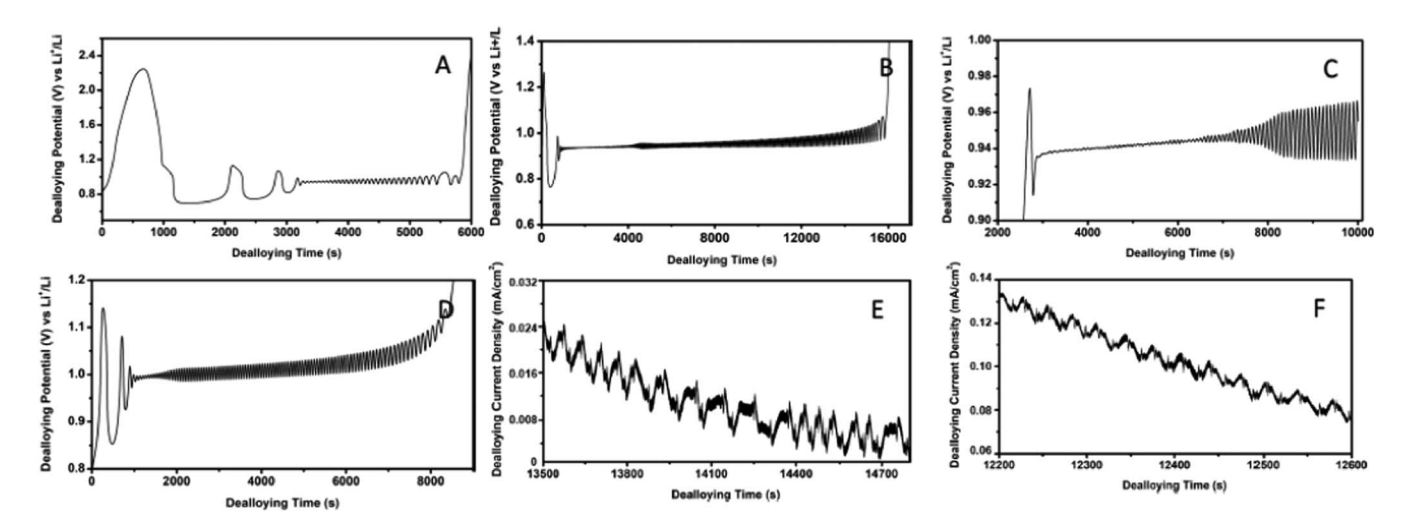


Figure 5. Morphology evolution under galvanostatic dealloying conditions and corresponding chronopotentiometry A.  $\text{Li}_3\text{Pb/Li}_7\text{Pb}_2$  at 500  $\mu\text{A}$  mA/cm²; negative dendrites B.  $\text{Li}_8\text{Pb}_3$  at 0.8 mAcm<sup>-2</sup>; nanoporous void nodule C.  $\text{Li}_8\text{Pb}_3$  at 10 mAcm<sup>-2</sup>; bi-continuous nanoporous structure D.  $\text{Li}_3\text{Pb/Li}_7\text{Pb}_2$  at 40 mA/cm²; anisotropic nanoporous structure. The corresponding chronopotentiometry is below the SEM images.



**Figure 6.** Electrochemical Oscillations during dealloying of Li-Pb alloys. Chronopotentiometry of A. LiPb/Li<sub>8</sub>Pb<sub>3</sub> at 1 mAcm<sup>2</sup>. Oscillation period  $\sim$ 70 s; Peak amplitude 130 mV. B. LiPb/Li<sub>8</sub>Pb<sub>3</sub> at 0.8 mAcm<sup>2</sup>. Oscillation period  $\sim$ 88 s; Peak amplitude 78 mV. C. Li<sub>8</sub>Pb<sub>3</sub> at 0.8 mAcm<sup>2</sup>. Oscillation period  $\sim$ 90 s; Peak amplitude 17 mV. D. Li<sub>7</sub>Pb<sub>2</sub> at 3 mAcm<sup>2</sup>. Oscillation period  $\sim$ 67 s; Peak amplitude 46 mV. chronocoulometry of E. LiPb/Li<sub>8</sub>Pb<sub>3</sub> at 1.0 V vs. Li<sup>+</sup>/Li F. LiPb/Li<sub>8</sub>Pb<sub>3</sub> at 1.0 V vs. Li<sup>+</sup>/Li.

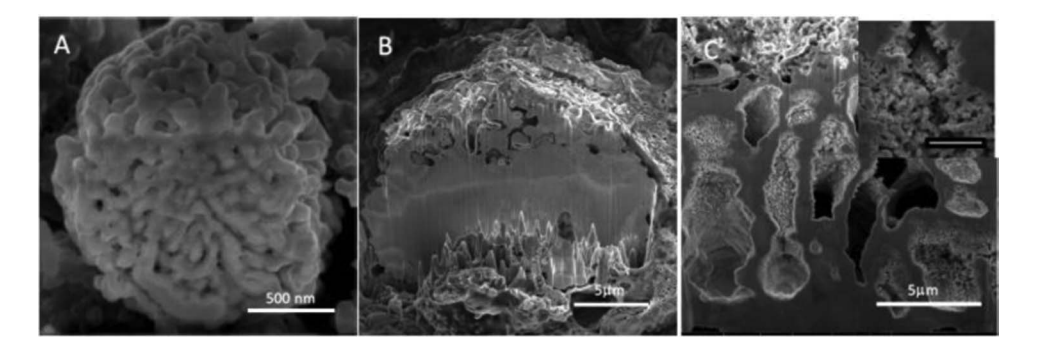


Figure 7. Size-effects on dealloyed morphology in the potentiostatic delithiation of Pb particles and sheets lithiated to 50 mV corresponding to the  $\text{Li}_7\text{Pb}_2$  composition A. 1  $\mu$ m diameter Pb particle delithiated at 1 V showing bicontinuous porosity. B. 15  $\mu$ m diameter Pb particle delithiated at 2 V showing negative dendrites. C. 15.2  $\mu$ m-thick Pb sheet delithiated at 2 V showing nanoporous void nodules (inset shows bicontinuous porosity on the walls of the void nodules with scale bar of 1  $\mu$ m).

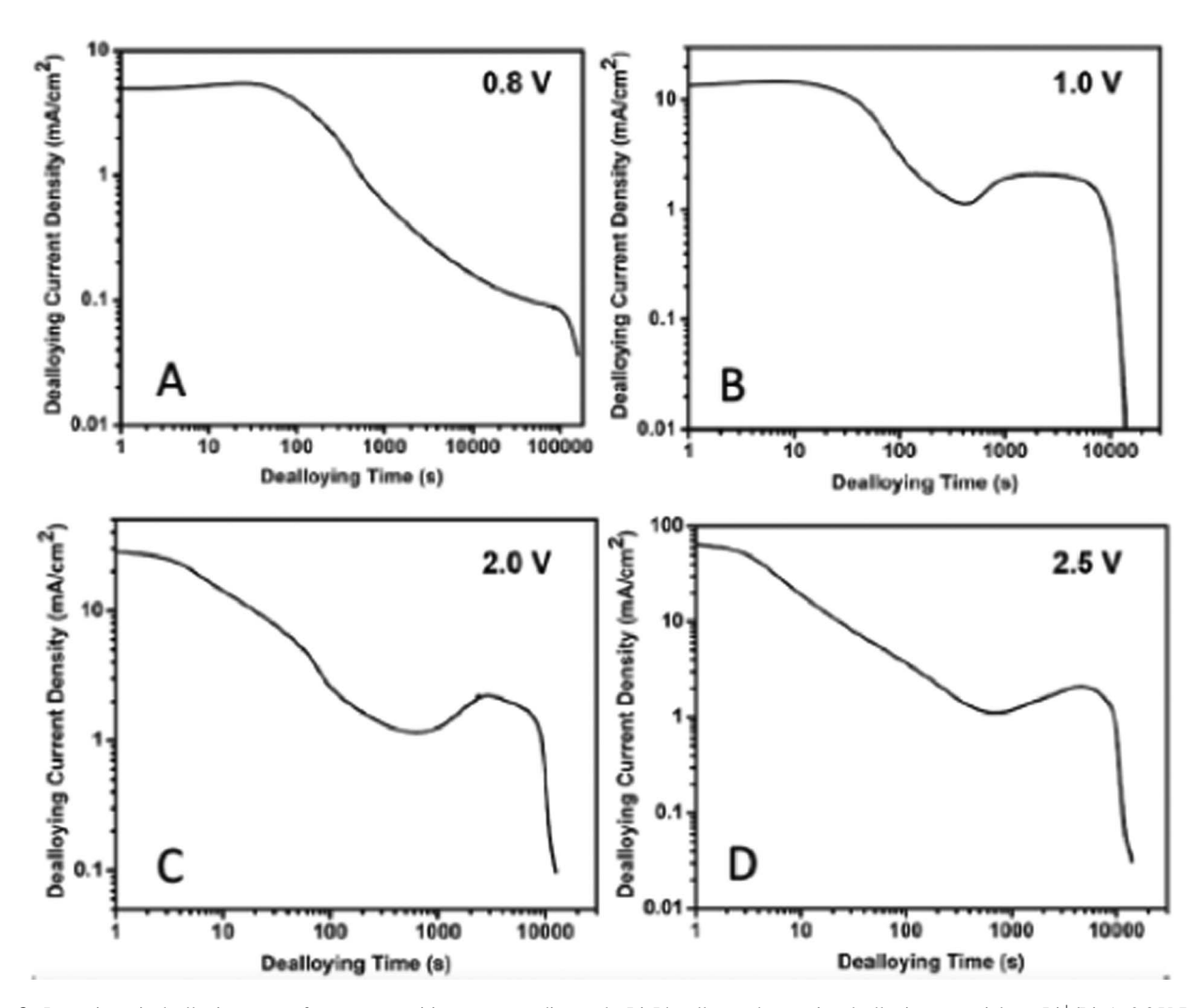


Figure 8. Potentiostatic dealloying curves from a composition corresponding to the  $Li_8Pb_3$  alloy under varying dealloying potentials vs.  $Li^+/Li$ . A. 0.8 V, B. 1.0 V, C. 2.0 V. D. 2.5 V.

the explanation likely relates to phase transitions occurring during the comparatively "low-rate" ( $< 10~\text{MAcm}^{-2}$ ) potentiostatic dealloying. Currently, we can only offer one possible explanation for the formation of the NVN morphology. When a single-phase Ag-Au alloy containing a sufficiently large silver concentration is dealloyed, remnants of a nanoporous structure are left at the bottom of the container, i.e., the structure is mechanically too fragile to hold together. Consider that the lithiated Pb sheet contains a two-phase microstructure. If percolation dissolution of the Pb-rich phase occurs resulting in a mechanical fragile morphology, collapse of this evolving structure could result in the development of holes with remnants of a nanoporous regions lining the walls of the holes, similar to our characterization of the NVN morphology.

The second surprise was the occurrence of electrochemical oscillations. As briefly described in the Introduction, there has only been one previous report of electrochemical oscillations related to Li dissolution which attributed the oscillations to a coupled "particle-by-particle" phase separation process.<sup>28</sup> Models of such a process have been developed for these "mosaic instabilities" and predict oscillatory-like behavior for slow Li-ion battery discharge rates (~C/1000 – C/100).<sup>29</sup> The experiments report that voltage oscillations begin at low amplitude, then grow in amplitude (1–10 mV) and eventually decay.<sup>28</sup> The porous-particulate form of the electrode is the key feature for the occurrence of these mosaic instability-based oscillations, so it is unclear how such a model would apply to the monolithic sheet electrodes for which we report oscillatory behavior. Consequently, the oscillations that we report on would appear to have a different origin. The voltage oscilla-

tions that we observe occurred at current densities of order 1 mAcm<sup>-2</sup> and ranged in amplitude from 33-130 mV. For our sheet samples, galvanostatic discharge at 1mAcm<sup>-2</sup> corresponds to a discharge rate of  $\sim$ 3C. Additionally, the voltage oscillations always initiated with large voltage spikes that eventually decayed into nearly fixed amplitude and period. Voltage (and current) oscillations during anodic dissolution of metal and alloys is not a new phenomenon and is most often associated with salt film precipitation and lift off.<sup>34</sup> The details of this depend on the identity of the metal electrode, the experimental set-up, the electrolyte composition, and the initial current or voltage-imposed dissolution conditions. In order to test the possible role of electrolyte composition, we performed ancillary experiments using 1M LiPF<sub>6</sub> in diethylene carbonate, dimethylene carbonate, ethylene carbonate in a 2:1:2 ratio by volume. For the range of current densities examined in these experiments (0.5-5 mAcm<sup>-2</sup>) we were unsuccessful in obtaining oscillatory behavior. There are two possible explanations for this. One is simply the difference in the solubility of LiClO<sub>4</sub> and LiPF<sub>6</sub> in the respective electrolytes, however, given the range of salt solubilities for which oscillations occur in other metal/electrolyte systems,34 we doubt that this can be the explanation. The other explanation is related to the detailed structure of the so-called solid-electrolyte interphase layer (SEI) that forms as a result of electrolyte breakdown. There is little doubt that the composition, detailed structure (coverage, porosity, etc.) and stability of the SEI layers formed in the two electrolytes are different although we made no attempt in this initial report of the oscillations to characterize these layers. Nevertheless, we suspect that in the 1 M LiClO<sub>4</sub> in polypropylene carbonate, the SEI layer promotes local salt-film precipitation events that become coupled over large enough length scales so as to make the voltage and current oscillations observable.

## Conclusions

The composition-dependent diffusion coefficient,  $\bar{D}_{Li}$ , obtained from both PITT and GITT during the dealloying of Li from Li-Pb alloys is  $10^{-12}$ – $10^{-10}$  cm<sup>2</sup>s<sup>-1</sup>, which is similar to that found for dealloying of Li from Li-Sn alloys. In the case of the 1 and 15 µm diameter Pb particles lithiated to 50 mV vs. Li<sup>+</sup>/Li and delithiated galvanostatically at various C-rates we obtained morphologies corresponding to Kirkendall voids, void nodules, negative dendrites and bi-continuous nanoporous structures. Under potentiostatic dealloying of 1 µm diameter Li<sub>7</sub>Pb<sub>2</sub> particles bicontinuous morphologies were observed. The mean ligament diameter in these nanoporous structures was  $\sim$ 50 nm. In the galvanostatic dealloying of 12.7 µm thick Li-Pb sheets, morphologies corresponding to nanoporous void nodules, negative dendrites and conventional large volume bicontinuous nanoporous morphologies were observed. Independent of composition, in the potentiostatic dealloying of lithiated Pb sheets, we were unable to obtain a full volume nanoporous morphology regardless of the applied voltage. For Pb sheet electrodes lithiated to at least 70 at.% Li, galvanostatic discharge at  $\sim$ 1 mAcm<sup>-2</sup> yielded voltage oscillations, while current oscillations were observed under potentiostatic dealloying at ~1.0 V vs. Li<sup>+</sup>/Li. We suggest that the source of these oscillations is salt film precipitation associated with the nature of the SEI layer formed on the electrode surface in the LiClO<sub>4</sub>/polypropylene carbonate electrolyte.

# Acknowledgment

The authors gratefully acknowledge the support of this work by the National Science Foundation, Division of Materials Research, under grants DMR-1306224 and DMR-1708459.

## **ORCID**

Karl Sieradzki https://orcid.org/0000-0002-4789-3956

## References

- 1. J. Erlebacher, M. J. Aziz, A. Karma, N. Dimitrov, and K. Sieradzki, "Evolution of nanoporosity in dealloying," Nature, 410(6827), 450 (2001).
- K. Sieradzki, N. Dimitrov, D. Movrin, C. McCall, N. Vasiljevic, and J. Erlebacher, The dealloying critical potential," J. Electrochem. Soc., 149(8), B370 (2002).
- 3. K. Sieradzki, R. R. Corderman, K. Shukla, and R. C. Newman, "Computer simulations of corrosion: selective dissolution of binary alloys," Philos. Mag. A, 59(4), 713 (1989).
- 4. K. Sieradzki, "Curvature effects in alloy dissolution," J. Electrochem. Soc., 140(10), 2868 (1993).
- 5. P. Mani, R. Srivastava, and P. Strasser, "Dealloyed Pt-Cu core- shell nanoparticle electrocatalysts for use in PEM fuel cell cathodes," J. Phys. Chem. C, 112(7), 2770
- J. Erlebacher, "Mechanism of coarsening and bubble formation in high-genus nanoporous metals," *Phys. Rev. Lett.*, 106(22), 225504 (2011).
- 7. H. W. Pickering, "Characteristic features of alloy polarization curves," Corros. Sci., 23 (10), 1107 (1983).
- A. J. Forty, "Corrosion micromorphology of noble metal alloys and depletion gilding," Nature, 282(5739), 597 (1979).

- 9. R. Li and K. Sieradzki, "Ductile-brittle transition in random porous Au," Phys. Rev. Lett., 68(8), 1168 (1992).
- 10. S. Sun, X. Chen, N. Badwe, and K. Sieradzki, "Potential dependent dynamic fracture of nanoporous gold", Nat. Mater., 14(9), 894 (2015).
- 11. J. Snyder, T. Fujita, M. W. Chen, and J. Erlebacher, "Oxygen reduction in nanoporous metal-ionic liquid composite electrocatalysts," Nat. Mater., 9(11), 904
- 12. V. R. Stamenkovic, B. S. Mun, K. J. J. Mayrhofer, P. N. Ross, and N. M. Markovic, "Effect of surface composition on electronic structure, stability, and electrocatalytic properties of Pt-transition metal alloys: Pt-skin versus Pt-skeleton surfaces," J. Am. Chem. Soc., 128(27), 8813 (2006).
- 13. V. R. Stamenkovic, B. S. Mun, M. Arenz, K. J. J. Mayrhofer, C. A. Lucas, G. Wang, P. N. Ross, and N. M. Markovic, "Trends in electrocatalysis on extended and nanoscale Pt-bimetallic alloy surfaces," Nat. Mater., 6(3), 241 (2007).
- 14. K. Hu, D. Lan, X. Li, and S. Zhang, "Electrochemical DNA biosensor based on nanoporous gold electrode and multifunctional encoded DNA- Au bio bar codes," Anal. Chem., 80(23), 9124 (2008).
- 15. Z. Matharu, P. Daggumati, L. Wang, T. S. Dorofeeva, Z. Li, and E. Seker, "Nanoporous Gold-Based Electrode Morphology Libraries for Investigating Structure-Property Relationships in Nucleic Acid-Based Electrochemical Biosensors," ACS Appl. Mater. Interfaces, 9, 12959 (2017).
- 16. C. A. R. Chapman, L. Wang, H. Chen, J. Garrison, P. J. Lein, and E. Seker, 'Nanoporous Gold Biointerfaces: Modifying Nanostructure to Control Neural Cell Coverage and Enhance Electrophysiological Recording Performance," Adv. Funct. Mater., 27, 1604631 (2016).
- 17. W.-C. Shih, G. M. Santos, F. Zhao, O. Zenasni, and M. M. P. Arnob, "Simultaneous Chemical and Refractive Index Sensing in the 1–2.5 μm Near-Infrared Wavelength Range on Nanoporous Gold Disks," Nano Lett., 16(7), 4641 (2016).
- 18. J. Biener, A. Wittstock, L. A. Zepeda-Ruiz, M. M. Biener, V. Zielasek, D. Kramer, R. N. Viswanath, J. Weissmuller, M. Baumer, and A. V Hamza, "Surface-chemistry driven actuation in nanoporous gold," Nat. Mater., 8(1), 47 (2009).
- C. Cheng, J. Weissmuller, and A. H. W. Ngan, "Fast and Reversible Actuation of Metallic Muscles Composed of Nickel Nanowire-Forest," Adv. Mater., 28(26), 5315 (2016).
- 20. H. Jin and J. Weissmuller, "Bulk nanoporous metal for actuation," Adv. Eng. Mater., 12(8), 714 (2010).
- 21. H.-J. Jin, X.-L. Wang, S. Parida, K. Wang, M. Seo, and J. Weissmuller, "Nanoporous Au- Pt alloys as large strain electrochemical actuators," Nano Lett., 10(1), 187
- 22. Ke Geng and K. Sieradzki, "Dealloying at High Homologous Temperature: Morphology Diagrams," J. Electrochem. Soc., 164(6), C330 (2017).
- 23. Q. Chen and K. Sieradzki, "Spontaneous evolution of bicontinuous nanostructures in dealloyed Li-based systems," *Nat. Mater.*, **12**(12), 1102 (2013).

  24. J. Sangster and C. W. Bale, "The Li-Sn (lithium-tin) system," *J. Phase Equilibria*,
- **19**(1), 70 (1988).
- 25. H. Okamoto, "Li-Pb (lithium-lead)," *J. Phase Equilibria* **14**(6), 770 (1993).
- 26. G. R. Goward, N. J. Taylor, D. C. S. Souza, and L. F. Nazar, "The true crystal structure of  $Li_{17}M_4$  M (M = Ge, Sn, Pb)–revised from  $Li_{22}M_5$ , " J. of Alloys and Compounds, 329(1-2), 82 (2001).
- 27. S. M. Wood, C. H. Pham, A. Heller, and C. B. Mullins, "Communication-Stages in the Dynamic Electrochemical Lithiation of Lead," J. Electrochem. Soc., 163(6), A1027 (2016).
- 28. D. Li, Y. Sun, Z. Yang, L. Gu, Y. Chen, and H. Zhou, "Electrochemical Oscillation in Li-Ion Batteries", Joule, 2(7), 1265 (2018).
- 29. T. R. Ferguson and M. Z. Bazant, "Nonequilibrium Thermodynamics of Porous Electrodes, J. Electrochem. Soc., 159(12), A1967 (2012).
- 30. Y. Wang and Y. Xia, "Bottom-up and top-down approaches to the synthesis of monodispersed spherical colloids of low melting-point metals," Nano Lett., 4(10)
- 31. C. J. Wen, B. A. Boukamp, R. A. Huggins, and W. Weppner, "Thermodynamic and Mass Transport Properties of 'LiAl," J. Electrochem. Soc., 126(12), 2258
- 32. W. Weppner and R. A. Huggins, "Determination of the Kinetic Parameters of Mixed-Conducting Electrodes and Application to the System Li<sub>3</sub>Sb," J. Electrochem. Soc., **124**(10), 1569 (1977).
- 33. M. A. V. Devanathan and Z. Stachurski, "The adsorption and diffusion of electrolytic hydrogen in palladium," in *Proceedings of the Royal Society of* London A: Mathematical, Physical and Engineering Sciences, 270(1340), 90 (1962).
- 34. J. L. Hudson and T. T. Tsotsis, "Electrochemical Reaction Dynamics: A Review," Chem. Eng. Sci., 49(10), 1493 (1994).